

Article

# Ni-Doped $\text{La}_{0.6}\text{Sr}_{0.4}\text{CoO}_3$ Perovskite as an Efficient Electrocatalyst for Oxygen Reduction and Evolution Reactions in Alkaline Media

Ronghua Yuan \*, Weina Xu, Liqun Pan, Ruibin Li, Chuanying Xiao and Xiaochang Qiao \*

School of Materials Science and Engineering, Dongguan University of Technology, Dongguan 523808, China

\* Correspondence: rhyuanrh@dgut.edu.cn (R.Y.); qiaoxc@dgut.edu.cn (X.Q.)

**Abstract:** The Co-based perovskite  $\text{La}_{0.6}\text{Sr}_{0.4}\text{CoO}_3$  has received significant attention as a potential electrocatalyst for its oxygen reduction reaction (ORR) and oxygen evolution reaction (OER) due to its abundance, facile synthesis, and high oxygen kinetics. However, research on the catalytic performance of Ni-doped  $\text{La}_{0.6}\text{Sr}_{0.4}\text{Co}_{1-x}\text{Ni}_x\text{O}_3$  as a bifunctional cathode catalyst for Zn-air batteries (ZABs) is still scarce. In this work, lanthanum strontium cobalt-based perovskite catalysts with various Ni contents ( $\text{La}_{0.6}\text{Sr}_{0.4}\text{Co}_{1-x}\text{Ni}_x\text{O}_3$ ,  $x = 0, 0.2, 0.5, \text{ and } 0.8$ ) were synthesized using a simple combustion method. The effects of Ni doping on the morphology, structure, surface oxygen-related species, and valence states of the transition metals of the perovskite were characterized. The electrochemical behaviors of the perovskite catalysts in both ORR and OER were also assessed. The characterization results revealed that proper Ni doping can decrease particle size, increase surface oxygen vacancies, and create mixed valence states of the transition metal and, thus, lead to improvement of the electrocatalytic activity of perovskite catalysts. Among the different perovskite compositions,  $\text{La}_{0.6}\text{Sr}_{0.4}\text{Co}_{0.8}\text{Ni}_{0.2}\text{O}_3$  exhibited the best ORR/OER activity, with a higher limiting current density, smaller Tafel slope, higher half-wave potential, lower overpotential, and lower potential difference than the other compositions. When  $\text{La}_{0.6}\text{Sr}_{0.4}\text{Co}_{0.8}\text{Ni}_{0.2}\text{O}_3$  was applied as the cathodic catalyst in a primary ZAB, it delivered a peak power density of  $81 \text{ mW cm}^{-2}$ . Additionally, in rechargeable ZABs, the  $\text{La}_{0.6}\text{Sr}_{0.4}\text{Co}_{0.8}\text{Ni}_{0.2}\text{O}_3$  catalyst exhibited a lower voltage gap (0.94 V) and higher stability during charge–discharge cycling than the commonly used catalyst Pt/C. These results indicate that Ni-doped  $\text{La}_{0.6}\text{Sr}_{0.4}\text{Co}_{0.8}\text{Ni}_{0.2}\text{O}_3$  is a promising bifunctional electrocatalyst for ZAB.

**Keywords:** Ni doping; perovskite; bifunctional electrocatalyst; oxygen reduction and evolution reaction; Zn-air battery



**Citation:** Yuan, R.; Xu, W.; Pan, L.; Li, R.; Xiao, C.; Qiao, X. Ni-Doped  $\text{La}_{0.6}\text{Sr}_{0.4}\text{CoO}_3$  Perovskite as an Efficient Electrocatalyst for Oxygen Reduction and Evolution Reactions in Alkaline Media. *Catalysts* **2023**, *13*, 1366. <https://doi.org/10.3390/catal13101366>

Academic Editors: Ting Zhang, Zhifu Liang and Xu Han

Received: 18 August 2023

Revised: 18 September 2023

Accepted: 19 September 2023

Published: 13 October 2023



**Copyright:** © 2023 by the authors. Licensee MDPI, Basel, Switzerland. This article is an open access article distributed under the terms and conditions of the Creative Commons Attribution (CC BY) license (<https://creativecommons.org/licenses/by/4.0/>).

## 1. Introduction

With the depletion of fossil fuels and with non-renewable energy sources becoming a pressing issue, there is an urgent need to search for new alternative energy sources and related energy conversion and storage devices [1–3]. In recent years, green, effective, and economical energy storage devices such as solar cells, lithium-ion batteries, and metal-air batteries have attracted significant attention from researchers [4–6]. Of the various devices, metal-air batteries, such as Zn-Air, Li-Air, and Al-Air batteries have been considered potential candidates for future energy applications [7–11]. Zn-Air batteries (ZABs) are of particular interest due to their many advantages, such as low cost, high efficiency, environmental friendliness, safe operation, and the abundance and stability of the metal zinc used in the anode [12–14]. The performance of ZABs is mainly determined by oxygen reduction reactions (ORRs) and oxygen evolution reactions (OERs) that occur on the cathode electrocatalyst. The slow reaction kinetics of the electrocatalysts have hindered the rapid development of ZABs [10,15]. Platinum-based, iridium-based, and ruthenium-based catalysts, which possess good catalytic performance, have been widely used as electrocatalysts in the past few decades, but they are limited in their application due to high

cost [16–19]. Noble metal electrocatalysts suffer from poor stability and limited performance during the cycling process in rechargeable ZABs [20–22]. Therefore, the development of new, inexpensive catalysts with excellent ORR/OER activity and durability is crucial for the commercialization of ZABs. For the last few decades, significant research efforts have been devoted to developing noble metal-free bifunctional electrocatalysts for ZABs, such as carbon-based materials, transition metal oxides, and perovskites [23–25].

Among the various kinds of catalysts, perovskites are considered promising bifunctional electrocatalysts because of their low cost and high electrocatalytic activity [26–28]. Perovskite-type oxide catalysts typically have a structural composition of  $ABO_3$ , where the A site is mostly composed of alkaline-earth (or rare-earth) metals, and the B site is occupied by transition metals. By partially replacing the A or B site cations, more oxygen vacancies can be generated, resulting in materials with excellent catalytic properties [29–31]. Among the different perovskites, lanthanum cobaltate ( $LaCoO_3$ ) has been considered a promising electrocatalyst due to its abundance, flexible crystal structure, and facile synthesis [32–34]. However, the limited number of active sites, low mixed ionic and electronic conductivity, and ordinary electrocatalytic activity of pristine  $LaCoO_3$  perovskite, in terms of efficiency and durability, limit its application in ZABs [33,35,36]. Various methods have been employed to enhance the electrocatalytic activity of  $LaCoO_3$  perovskites, including partially replacing the A- or B-site cations. For example, the A-site of  $LaCoO_3$  perovskite can be partially replaced by alkaline-earth metals (such as Ca or Ba) to increase the oxygen vacancy concentration and enhance the bifunctional electrocatalytic activity and stability of the perovskite oxide [36,37]. Doping Sr into  $LaCoO_3$  perovskite oxide can also improve the oxygen diffusion performance and increase the ionic conductivity, thus improving ORR and OER activity [38,39]. Although A-site doping perovskites, such as  $La_{0.6}Sr_{0.4}CoO_3$ , possess good OER activity, the catalytic performance of the ORRs is insufficient. Doping in the B-site of perovskite may also be an effective approach. Chandrappa et al. investigated the catalytic properties of  $LaCoO_3$  with the B-site cation occupied by Ru. The obtained catalyst exhibited excellent bifunctional electrocatalytic activity in ZABs [35]. Wang et al. explored the evolution of the ORR mechanism of Fe substitution into  $LaCoO_3$ , and enhanced catalytic activities and increased electron transfer numbers during the ORR were observed [40]. Vignesh et al. reported that the substitution of proper Co by Ni in  $LaCo_{0.97}O_{3-\delta}$  porous nanostructures can greatly alter the electrocatalytic activity and reveal superior charge and discharge potentials in ZABs [41]. Zhang et al. found that Nb doping in  $La_{0.2}Sr_{0.8}CoO_{3-\delta}$  is detrimental to OER activity but benefits cycling stability [42]. Sun et al. demonstrated trace Ni-doped  $La_{0.6}Sr_{0.4}CoO_3$  perovskites were higher-performance catalysts for both ORRs and OERs by cyclic voltammetry measurements, and they were further used as catalysts for  $Li-O_2$  batteries using a non-aqueous electrolyte. Although various research has been reported concerning the catalytic activity of  $LaCoO_3$ -based perovskites, there are still no comprehensive reports on the ORR and OER activity of Ni-doped  $La_{0.6}Sr_{0.4}CoO_3$  perovskites in alkaline solutions.

In this work, we synthesized the Ni-doped lanthanum strontium cobalt perovskite  $La_{0.6}Sr_{0.4}Co_{(1-x)}Ni_xO_3$  ( $x = 0, 0.2, 0.5, \text{ and } 0.8$ ), using a simple method, to act as the bifunctional electrocatalyst. To reveal the mechanism of Ni doping, X-ray diffraction (XRD), scanning electron microscopy (SEM), transmission electron microscopy (TEM), and X-ray photoelectron spectroscopy (XPS) were employed to observe the crystal structure, surface morphology, and oxygen vacancy concentration of the perovskite oxides. The electrocatalytic activities of the perovskites were evaluated in an alkaline medium, and the optimal Ni doping level was determined. The perovskite catalyst with optimal Ni doping was then applied in a ZAB to assess its bifunctional activity as a cathode catalyst. The perovskite catalyst exhibited excellent activity and durability compared to Pt/C, suggesting its potential application in ZABs.

## 2. Results and Discussion

The XRD patterns shown in Figure 1 exhibited the phase structure of the as-prepared  $\text{La}_{0.6}\text{Sr}_{0.4}\text{Co}_{1-x}\text{Ni}_x\text{O}_3$  ( $x = 0, 0.2, 0.5, 0.8$ ) perovskite catalysts. For the LSC sample ( $x = 0$ ), the diffraction peaks were located at  $23.2^\circ$ ,  $33^\circ$ ,  $40.7^\circ$ ,  $47.4^\circ$ ,  $59^\circ$ , and  $69.4^\circ$ , which could be indexed to a rhombohedral perovskite phase  $(\text{LaSr})(\text{CoNi})\text{O}_3$ . When the Ni concentration was 0.2, the diffraction peaks were the same as those of LSC, indicating that the Ni had fully integrated into the perovskite structure to form a rhombohedral structure. However, when the Ni content was further increased to 0.5 and above, some other phases gradually appeared in the sample. In addition to the rhombohedral perovskite phase, a small amount of tetragonal phase  $(\text{LaSr})\text{NiO}_4$  and NiO were detected. This indicated that, when the Ni content is high, the structural stability of the perovskite formed is compromised, leading to decomposition and the formation of NiO. The produced NiO can then dissolve into the perovskite sample to form the tetragonal phase  $(\text{LaSr})\text{NiO}_4$ . These findings were consistent with previous results from other researchers [2,28,43].

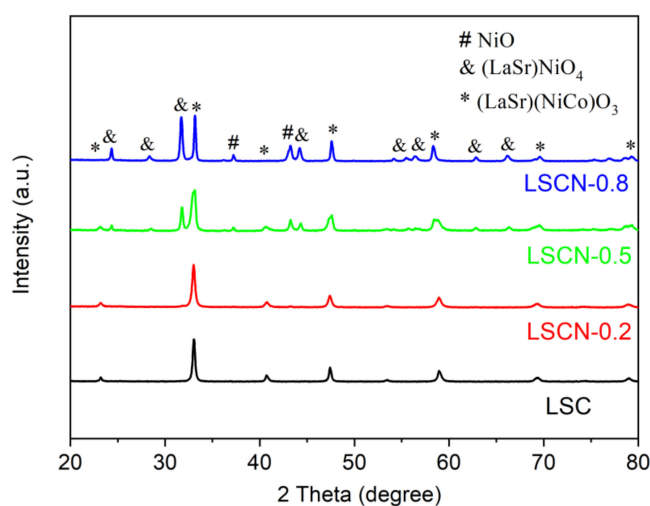


**Figure 1.** XRD patterns for LSC, LSCN–0.2, LSCN–0.5, and LSCN–0.8.

The SEM images of the perovskite catalysts are presented in Figure 2, revealing that the prepared perovskite catalysts consisted of irregular particles. The particle sizes of the perovskite catalysts increased as the doping amount of Ni increased. For example, for the LSC particle, the size distribution ranged from about 20 to 80 nm. When the Ni content was 0.2 (LSCN–0.2), the catalyst particle size slightly enlarged to 30 to 100 nm. With further increases in Ni content, the catalyst particle sizes significantly increased to 80 to 200 nm and 100 to 250 nm for LSCN–0.5 and LSCN–0.8, respectively. The larger particle sizes of the perovskite catalysts can be attributed to the sintering aid provided by Ni. It is evident that the primary particles further aggregated with other particles to form larger secondary particles. The size of the secondary particles also increased with increasing Ni content.

To investigate the internal microstructure and element distribution of perovskite catalysts, TEM characterization was performed. The TEM image for the representative LSCN–0.2 perovskite catalyst is shown in Figure 3a, revealing that the particle size was below 100 nm, which was consistent with Figure 2. Additionally, the small particles were in intimate contact with other particles, which may facilitate the mass transfer rate and thus enhance the electrocatalytic activity. The representative HRTEM image of the LSCN–0.2 perovskite catalyst is displayed in Figure 3b. The interplanar spacing of LSCN–0.2 was 0.38 nm, indexing to the (100) plane, which was also in agreement with the XRD pattern results. The TEM-EDS elemental mapping images, as shown in Figure 3c, indicated uniformly distributed La, Sr, Co, Ni, and O elements in LSCN–0.2, confirming that Ni was present in the solid solution, occupying the Co position. This further demonstrated the successful incorporation of Ni into the perovskite lattice structure.

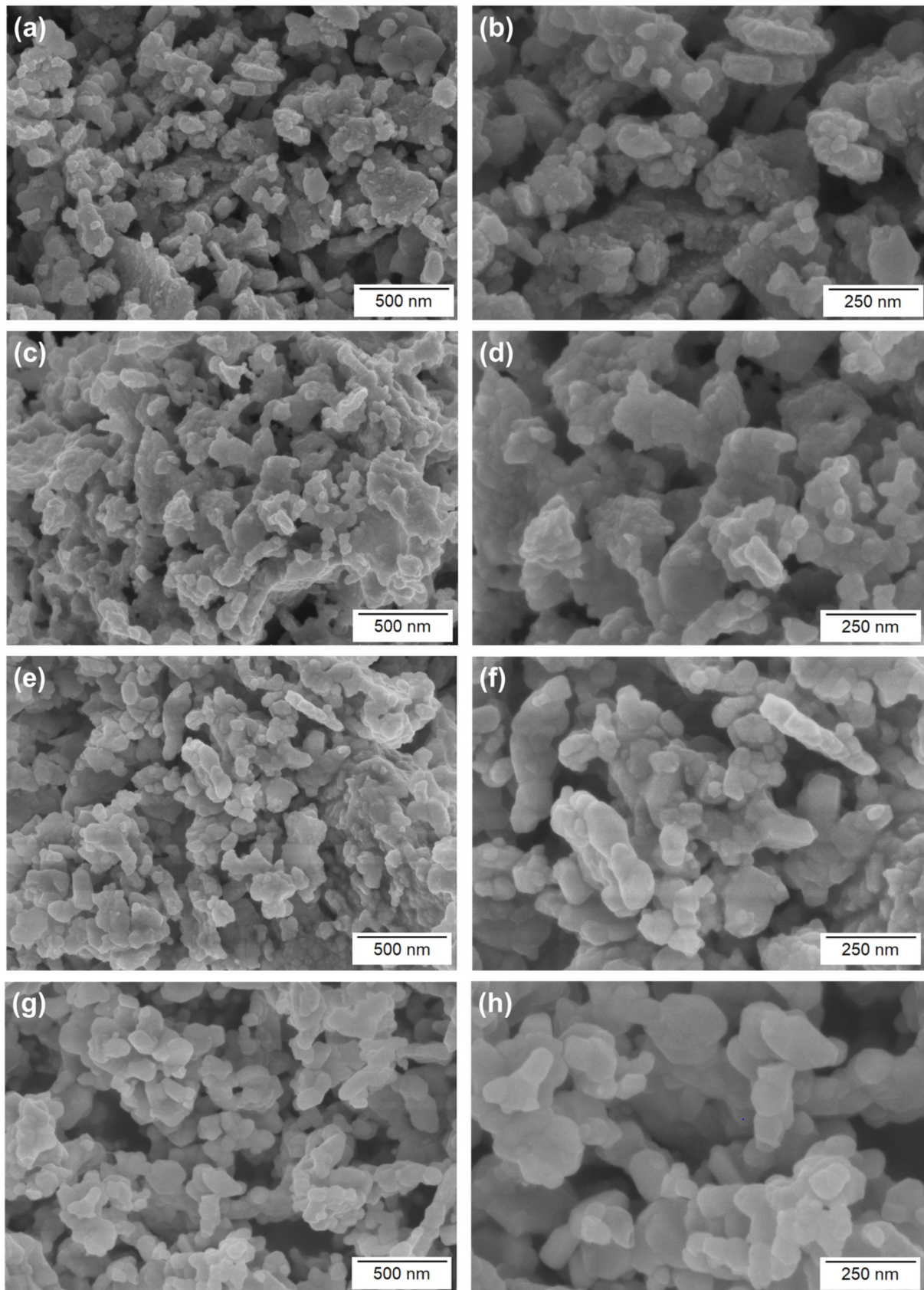


**Figure 2.** SEM micrograph of perovskite catalysts with different Ni contents: (a,b) LSC, (c,d) LSCN-0.2, (e,f) LSCN-0.5, (g,h) LSCN-0.8.

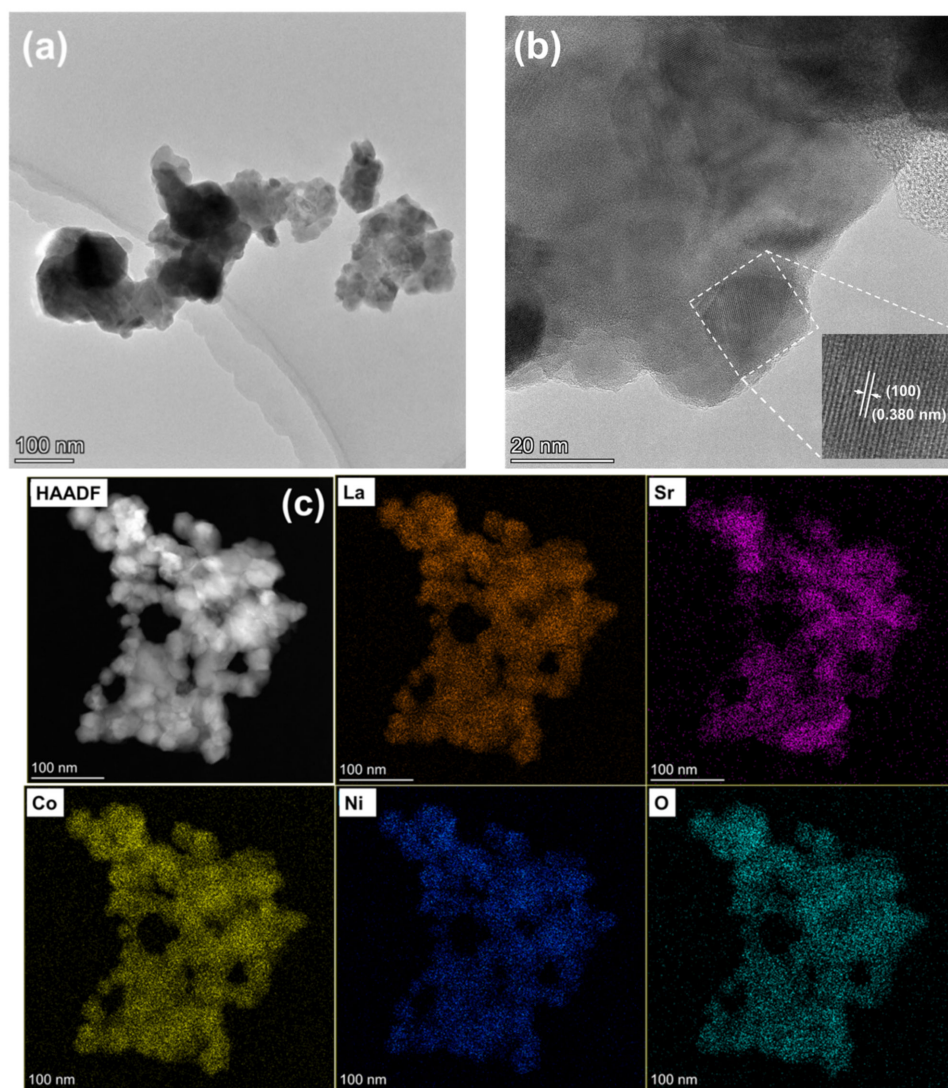


**Figure 3.** (a,b) TEM and HRTEM images of LSCN-0.2; (c) HAADF-STEM image of LSCN-0.2 and the corresponding EDS mapping image.

XPS analysis was conducted to investigate the influence of surface oxygen species and transition metal valence states on the ORR and OER performance of the perovskite catalysts. The spectra are displayed in Figure 4. The full XPS spectra in Figure 4a demonstrate the presence of La 3d, Sr 3d, Co 2p, Ni 2p, and O 1s peaks, confirming the coexistence of La, Sr, Co, Ni, and O elements. This was consistent with the TEM-EDS results. Figure 4b displays the O1s spectra, in which four peaks can be observed. These peaks can be attributed to lattice oxygen (528 eV),  $\text{O}_2^{2-}/\text{O}^-$  (529.8 eV),  $\text{O}_2/\text{OH}^-$  (531 eV), and adsorbed  $\text{H}_2\text{O}/\text{CO}_2$  (532.7 eV), respectively. Oxygen vacancies are typically associated with surface  $\text{O}_2^{2-}/\text{O}^-$  species, which are reactive species for oxygen-related reactions [44,45]. The concentration of  $\text{O}_2^{2-}/\text{O}^-$  species was calculated for the four perovskite catalysts. For undoped LSC, the concentration of  $\text{O}_2^{2-}/\text{O}^-$  species was 18.1%. It increased to 26.9% for LSCN-0.2, then decreased significantly to 12.8% for LSCN-0.5 and 11.4% for LSCN-0.8, as NiO began to dissolve out. The relatively higher concentration of  $\text{O}_2^{2-}/\text{O}^-$  species in LSCN-0.2 may contribute to better ORR and OER activities. The Co and Ni oxidation states were also analyzed by XPS, as shown in Figure 4c,d. In the Co 2p spectra, the main peaks located at around 779.9 eV and 794.9 eV could be attributed to Co 2p 3/2 and Co 2p 1/2, respectively. Each of these peaks could be further divided into two peaks. The peaks at the binding energies of 779.7 eV and 794.8 eV represented  $\text{Co}^{3+}$ , and the others near 781.2 eV and 796.2 eV corresponded to  $\text{Co}^{2+}$ . This suggested the coexistence of  $\text{Co}^{2+}$  and  $\text{Co}^{3+}$  mixed

valence states. Due to the strong overlap of Ni 2p and La 3d peaks, quantifying the nickel content from the Ni 2p 2/3 peak was challenging. However, it could be achieved using the main Ni 2p 1/2, which could be deconvoluted into two peaks located at 871.7 eV and 873.7 eV, corresponding to Ni<sup>2+</sup> and Ni<sup>3+</sup>, as shown in Figure 4d. This indicated the coexistence of Co<sup>3+</sup>, Co<sup>2+</sup>, Ni<sup>2+</sup>, and Ni<sup>3+</sup> valence states, which may promote the generation of oxygen vacancies and contribute to the improvement of ORR and OER activities.

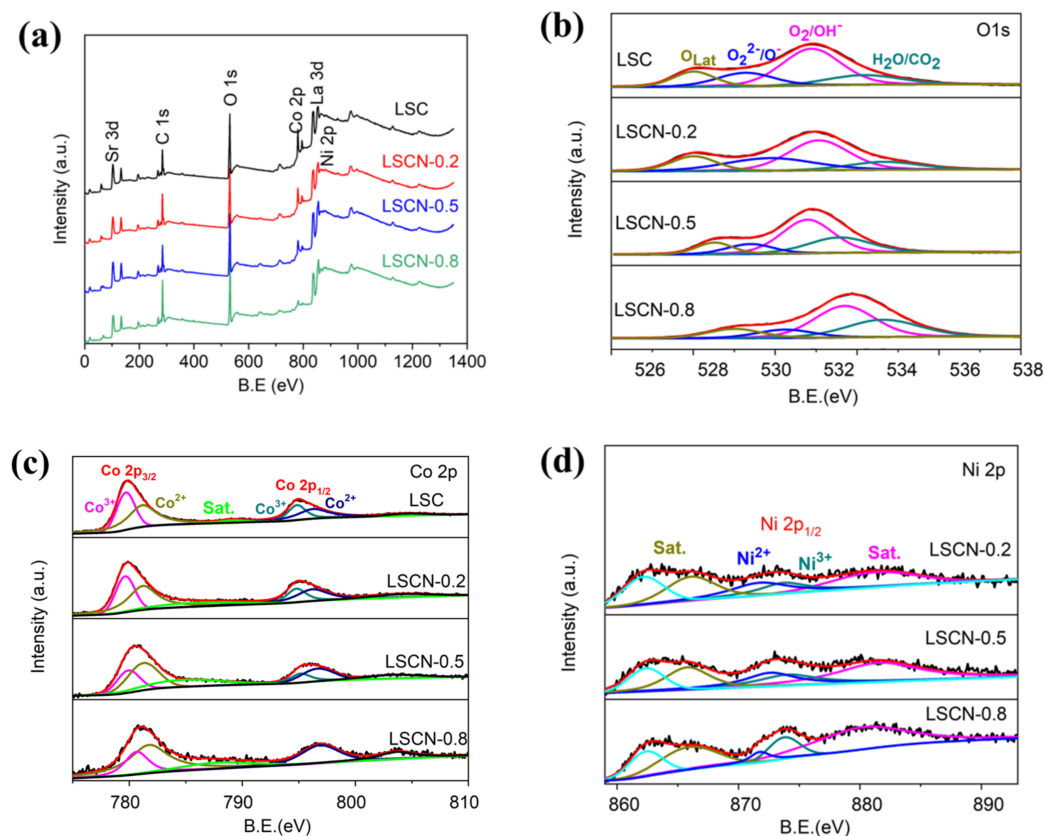


**Figure 4.** XPS spectra of LSC, LSCN–0.2, LSCN–0.5, and LSCN–0.8: (a) survey scan; (b) O 1s; (c) Co 2p; and (d) Ni 2p.

The ORR activities of the perovskite catalysts were investigated by a three-electrode test system with an O<sub>2</sub>-saturated 0.1 M KOH electrolyte. Figure 5 shows the LSV and Tafel curves of the perovskite catalysts with different Ni contents. In Figure 5a, the onset potential (the potential corresponding to the 5% limit current density) of LSC was –0.164 V vs. Ag/AgCl. When 20% of the Co in LSC was replaced by Ni, the onset potential shifted positively to –0.142 V vs. Ag/AgCl, which was the highest among all the samples. For LSCN–0.5 and LSCN–0.8, the onset potential values were –0.181 V vs. Ag/AgCl and –0.223 V vs. Ag/AgCl, respectively. The half-wave potential ( $E_{1/2}$ ) also followed this trend. Furthermore, the limiting current densities of the perovskite catalysts ranged between 4.95 mA cm<sup>–2</sup> and 5.73 mA cm<sup>–2</sup>, with LSCN–0.2 exhibiting the highest limiting current density of 5.73 mA cm<sup>–2</sup>, which was closest to that of Pt/C (6.39 mA cm<sup>–2</sup>). LSC and LSCN–0.5 had similar limiting current densities, while LSCN–0.8, with the highest Ni doping level, displayed the lowest limiting current density of 4.95 mA cm<sup>–2</sup>. The corresponding Tafel slopes are shown in Figure 5b, and they followed this trend: LSCN–0.2 > LSCN–0.5 > LSC > LSCN–0.8. Clearly, LSCN–0.2 exhibited the smallest Tafel slope among all the samples, indicating the best ORR electrocatalytic activity. The stability of the LSCN–0.2 and Pt/C catalyst was studied under ORR conditions by CA at 1600 rpm and –0.4 V vs. Ag/AgCl. The results are displayed in Figure 5c. As expected, the LSCN–0.2 catalyst exhibited better long-term stability, with a 4.5% current loss for

over 10,000 s. However, for the Pt/C catalyst, the current density rapidly declined at the beginning of the test, and finally, a current loss of 11.3% was obtained. The above results suggest that a moderate amount of Ni doping can enhance the ORR activity, but a high proportion of doping may reduce the catalytic performance in terms of ORRs.

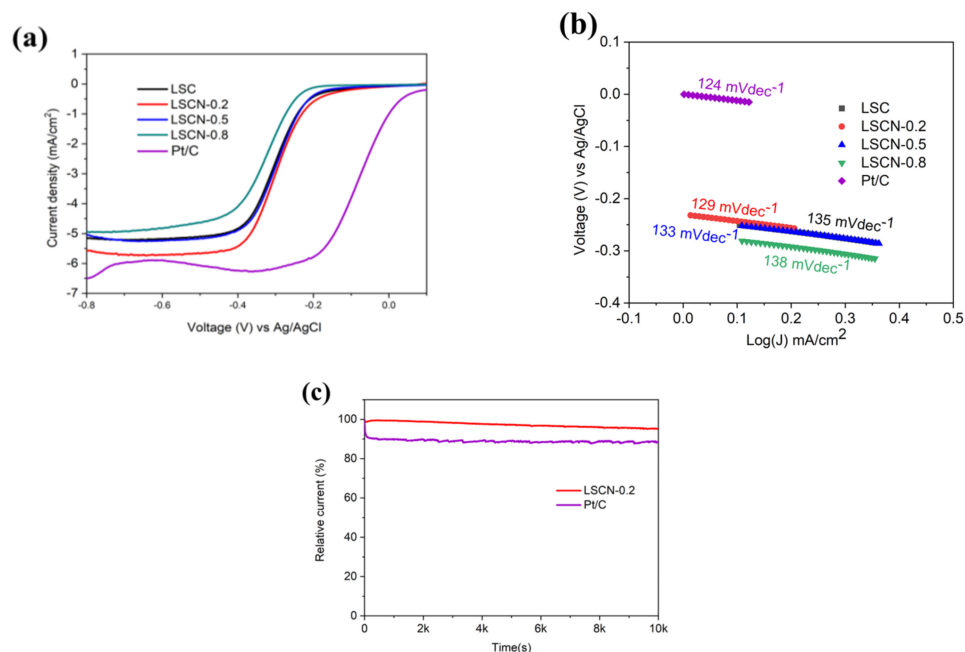


**Figure 5.** (a) LSV curves of ORR for LSC, LSCN–0.2, LSCN–0.5, LSCN–0.8, and Pt/C; (b) the corresponding Tafel plots for LSC, LSCN–0.2, LSCN–0.5, LSCN–0.8, and Pt/C; (c) CA of LSCN–0.2 and Pt/C under the ORR condition maintained at  $-0.4$  V vs. Ag/AgCl for 10,000 s.

In addition to ORRs, the OER activity is also crucial for an efficient bifunctional catalyst. Figure 6a,b present the LSV curves and Tafel slopes for OERs of perovskite catalysts with different Ni doping levels. A lower overpotential ( $E_{j10}$ ) typically indicates better OER activity. Among the four perovskite catalysts, LSCN–0.2 exhibited the lowest overpotential of 0.83 V vs. Ag/AgCl. The overpotential increased to 0.863 V, 0.845 V, and 0.879 V vs. Ag/AgCl for LSC, LSCN–0.5, and LSCN–0.8, respectively. At 1 V vs. Ag/AgCl, the current density followed the order: LSCN–0.2 ( $23.2 \text{ mA cm}^{-2}$ ) > LSCN–0.5 ( $20.6 \text{ mA cm}^{-2}$ ) > LSC ( $19 \text{ mA cm}^{-2}$ ) > LSCN–0.8 ( $16.9 \text{ mA cm}^{-2}$ ). The Tafel slope of LSCN–0.2 was  $209 \text{ mVdec}^{-1}$ , which was the smallest among the four catalysts. The smallest Tafel slope, together with the lowest overpotential and highest current density, indicated the superior OER activity of LSCN–0.2. Figure 6c shows the EIS measurements conducted at 1 V vs. Ag/AgCl for all the catalysts. The electrode resistance for charge-transfer,  $R_c$ , represented by the diameter of the semicircle, was smallest for LSCN–0.2, indicating faster charge transfer during OERs. These results demonstrated that LSCN–0.2, with the appropriate Ni doping ratio, exhibited the best OER activity, consistent with the ORR results. CA measurements under OER conditions at 0.7 V vs. Ag/AgCl were conducted to explore the stability of LSCN–0.2 and Pt/C (Figure 6d). The current retention of LSCN–0.2 was significantly higher than that of Pt/C. To evaluate the bifunctional activity of the perovskites, overall LSV curves of  $-0.8$ – $1.0$  V vs. Ag/AgCl were obtained, as shown in Figure 6e. The potential difference calculated by  $\Delta E = E_{j10} - E_{1/2}$  is displayed in Figure 6f. LSCN–0.2 exhibited the smallest  $\Delta E$  value of 1.126 V, suggesting excellent ORR/OER reversibility. The optimal performance of LSCN–0.2 can mainly be attributed to the slightly higher surface oxygen vacancies caused by Ni doping, as analyzed in the XPS results. However, when the Ni doping level was too high, the surface-precipitated NiO hampered the transport of reaction electrons, resulting in a decrease in electrocatalytic activity.

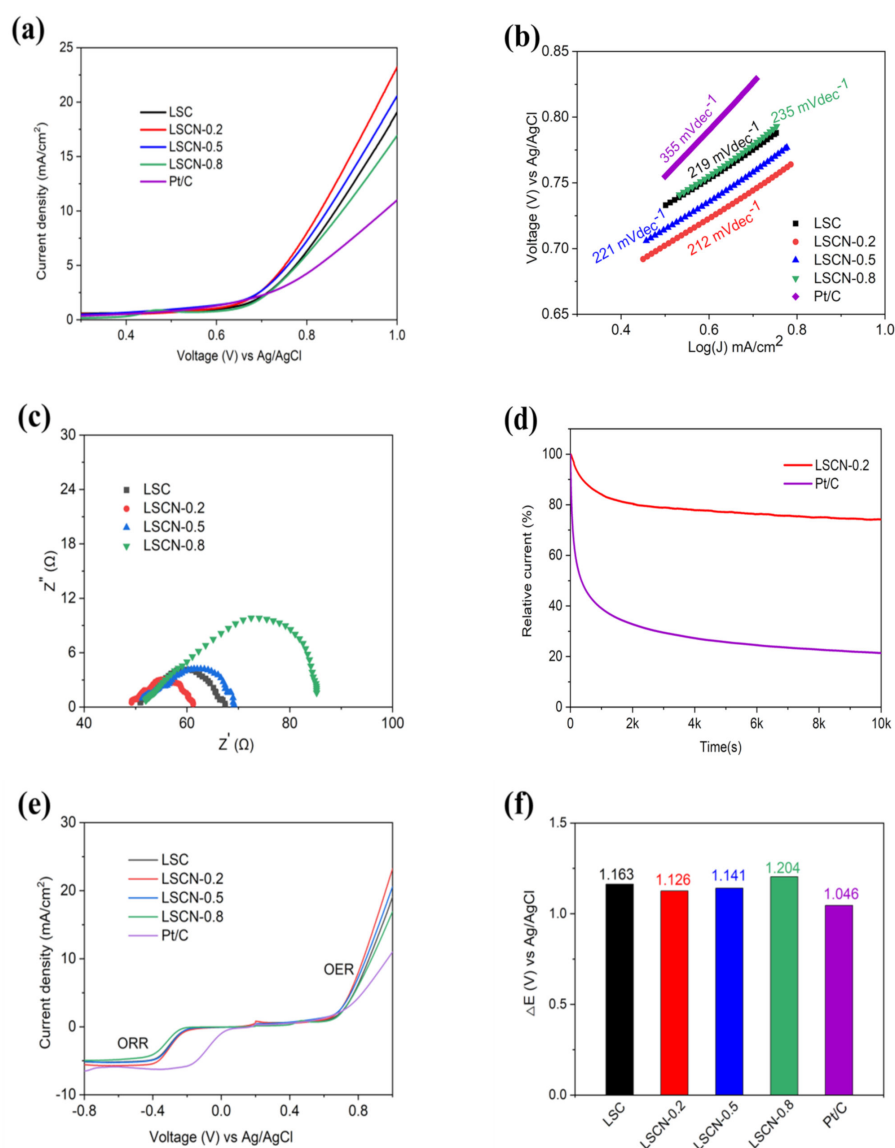


**Figure 6.** (a) OER LSV curves of LSC, LSCN–0.2, LSCN–0.5, LSCN–0.8, and Pt/C. (b) OER Tafel plots for LSC, LSCN–0.2, LSCN–0.5, LSCN–0.8, and Pt/C catalysts. (c) EIS plots at 1.0 V vs. Ag/AgCl. (d) CA of LSCN–0.2 and Pt/C under OER conditions maintained at 0.7 V vs. Ag/AgCl for 10,000 s. (e) The overall LSV curves of –0.8–1.0 V vs. Ag/AgCl. (f) The values of  $\Delta E$  ( $\Delta E = E_{j10} - E_{j1/2}$ ).

Based on the analysis of the ORR and OER performance, the LSCN–0.2 catalyst exhibited the best overall performance. To further assess its practicality, we applied it as the cathode catalyst in a homemade ZAB, with the Pt/C catalyst as the benchmark. Figure 7a represents the I–V–P curves of the prepared primary batteries. The peak power density of the primary battery using LSCN–0.2 as the cathode catalyst was 81 mW/cm<sup>2</sup>, which was lower than the Pt/C catalyst (111 mW cm<sup>-2</sup>). This suggested that, although the LSCN–0.2 catalyst demonstrated superior electrocatalytic activity among the perovskite catalysts, its discharge performance still needs improvement compared to precious metal catalysts like Pt/C. However, the LSCN–0.2 catalyst exhibited better durability compared to Pt/C. Figure 7b displays the cycling performance of the batteries evaluated at 10 mA cm<sup>-2</sup>, with each cycle lasting for ten minutes. During the first cycle, the LSCN–0.2 electrode exhibited a lower discharge voltage of ~1.16 V and a charge voltage of ~2.10 V. In comparison, the discharge voltage and charge voltage for Pt/C were 1.23 V and 2.3 V, respectively. This resulted in a voltage gap of 0.94 V for LSCN–0.2 and 1.07 V for Pt/C. Additionally, the LSCN–0.2 catalyst displayed better durability compared to Pt/C, with stable charge and

discharge voltages for over 80 cycles. On the other hand, the discharge voltage of the Pt/C catalyst rapidly decreased after 20 cycles. Overall, the LSCN-0.2 catalyst showed promise as a candidate for rechargeable ZABs. Although its discharge performance needs improvement compared to Pt/C, it exhibited better durability and cycling stability. Further optimization and refinement of the LSCN-0.2 catalyst could enhance its performance and make it a viable alternative to precious metal catalysts in ZAB applications.

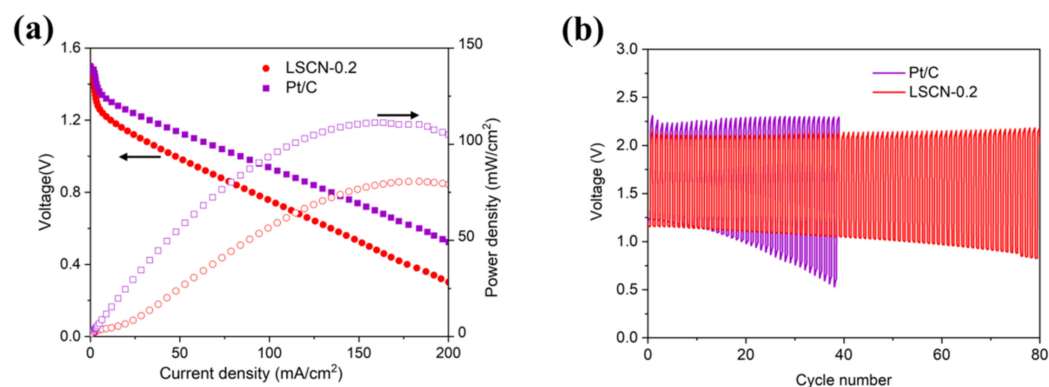


**Figure 7.** (a) I-V-P curves of the prepared primary ZABs with LSCN-0.2 and Pt/C as the cathode catalyst. (b) Charge and discharge curves of rechargeable ZABs with LSCN-0.2 and Pt/C as the cathode catalyst.

### 3. Conclusions

In summary, we synthesized a series of lanthanum strontium cobalt-based perovskites with different levels of Ni doping. We characterized the morphology, surface oxygen-related species, and valence states of the transition metal in the catalysts, and we evaluated their electrochemical performance for both ORRs and OERs. Our electrochemical measurements showed that  $\text{La}_{0.6}\text{Sr}_{0.4}\text{Co}_{0.8}\text{Ni}_{0.2}\text{O}_3$  exhibited superior electrocatalytic activity compared to the other perovskite catalysts. It had a higher limiting current density, smaller Tafel slope, higher half-wave potential, lower overpotential, and smaller electrode resistance. The potential difference between the overpotential and half-wave potential was also the smallest for this catalyst. The enhanced electrocatalytic activity of  $\text{La}_{0.6}\text{Sr}_{0.4}\text{Co}_{0.8}\text{Ni}_{0.2}\text{O}_3$  may be attributed to the slightly higher number of surface oxygen vacancies caused by appropriate Ni doping. This catalyst was further tested in a homemade primary zinc-air battery (ZAB) as the cathode catalyst and delivered a peak power density of approximately  $81 \text{ mWcm}^{-2}$ . Moreover, when used as the catalyst in a rechargeable ZAB,  $\text{La}_{0.6}\text{Sr}_{0.4}\text{Co}_{0.8}\text{Ni}_{0.2}\text{O}_3$  demonstrated better cycling stability and a lower voltage gap. These promising results indicate that proper Ni doping in lanthanum strontium cobalt-based perovskites is an effective strategy for producing efficient and durable bifunctional catalysts for rechargeable ZABs.

### 4. Experiments

#### 4.1. Preparation of the Perovskite Catalyst

$\text{La}_{0.6}\text{Sr}_{0.4}\text{Co}_{1-x}\text{Ni}_x\text{O}_3$  ( $x = 0, 0.2, 0.5, \text{ and } 0.8$ ) perovskites, denoted as LSC, LSCN-0.2, LSCN-0.5, and LSCN-0.8, were synthesized by a combustion method. Firstly, we dissolved an appropriate amount of  $\text{La}(\text{NO}_3)_3$ ,  $\text{Sr}(\text{NO}_3)_2$ ,  $\text{Co}(\text{NO}_3)_2 \cdot 6\text{H}_2\text{O}$ , and  $\text{Ni}(\text{NO}_3)_2 \cdot 6\text{H}_2\text{O}$  as the raw materials in 100 mL of DI water. Then, citric acid and glycine were added as combustion fuel to the metal nitrate solution. The mole ratio of metal ions/citric acid/glycine was maintained at 1:2:1. The pH of the mixed solution was adjusted to approximately 8.00 by adding an appropriate amount of ammonia. After that, the solution was stirred for 1 h to ensure proper mixing. Then, we heated the solution gradually until combustion occurred and collected the black precursor. Finally, the black precursor was sintered at  $900 \text{ }^\circ\text{C}$  for 4 h in a furnace to obtain the desired perovskite powder.

#### 4.2. Characterization of Perovskite Catalysts

The phase structure and composition of the synthesized perovskite catalysts were analyzed using the XRD technique (Rigaku SmartLab SE, Tokyo, Japan). The morphology and element distribution of the perovskite catalysts were characterized using both SEM (ZEISS VO-MA10, Oberkochen, Germany) and TEM (FEI Talos F200s, Hillsboro, OR, USA). Additionally, an energy dispersive X-ray spectroscopy (EDS) device was used in combination with SEM and TEM to assess the distribution of elements on the catalysts' surfaces. To analyze the surface active sites of the perovskite catalysts, the XPS technique was used (Thermo Scientific K-Alpha, Waltham, MA, USA). XPS provides information about the chemical state of elements present on the catalysts' surfaces.

#### 4.3. Electrochemical Measurements

The ORR and OER activities of the perovskite catalysts were measured using a three-electrode test device attached to an electrochemical station (CHI 760). The three-electrode test device consisted of a counter electrode (platinum foil), a reference electrode (saturated Ag/AgCl), and a working electrode (glass-carbon). The working electrode was prepared as follows: perovskite catalyst (2.5 mg) and conductive Vulcan-XC72 carbon (Birmingham, AL, USA) (2.5 mg) were first distributed in 0.25 mL isopropanol; then, 0.05 mL of 5 wt.% Nafion solution was added to the mixed solution as a binder. The mixture was then treated with an ultrasound for 1 h to obtain a uniform ink. Using a pipette gun, a certain amount of the catalyst ink was removed and coated onto the glass-carbon electrode. The electrode was then dried naturally in ambient air to form a homogeneous film. The effective area of the film was 0.196 cm<sup>2</sup>, and the catalyst loading amount was 0.2 mg cm<sup>-2</sup>. Meanwhile, commercial Pt/C (20 wt.%, Aladdin Corp. Bay City, MI, USA) catalyst ink was also prepared to evaluate the ORR and OER activities. Before the measurement, pure oxygen was bubbled directly into the electrolytic cell containing a 0.1 M KOH solution as the electrolyte for more than 30 min. Throughout the tests, oxygen was continuously vented into the electrolyte solution. Linear sweep voltammetry (LSV) experiments were performed at a rotating speed of 1600 rpm and a scan rate of 10 mV/s. Electrochemical impedance spectroscopy (EIS) analysis was conducted at a frequency range from 0.1 Hz to 10<sup>5</sup> Hz, with an amplitude of 10 mV, at a potential of 1 V versus the Ag/AgCl reference electrode. Finally, stability tests were conducted at fixed potentials and rotation speeds of 1600 rpm by using chronoamperometry (CA) measurements.

#### 4.4. Preparation and Tests of the Zn-Air Battery

The optimal Ni doping perovskite catalyst was applied as the cathode catalyst on a homemade ZAB to evaluate its practicality as a bifunctional electrocatalyst. To prepare the cathode catalyst, 5 mg of perovskite powder, 10 mg of Vulcan-XC72 carbon, and 0.1 mL of 5 wt.% Nafion solution were mixed in 1 mL of ethanol. The catalyst mixture was continuously magnetically stirred for 2 h, and then it was painted onto carbon paper using an airbrush. The coated carbon paper was dried in an oven for ten minutes. The painting process was repeated several times to achieve a loading amount of 2 mg cm<sup>-2</sup> of the catalysts on the carbon paper. Then, a gas diffusion layer and a current collection layer, together with the catalyst layer, formed the cathode electrode. In addition to the three-layer cathode structure, a piece of Zn plate and a 6 M KOH solution were used as the anode and electrolyte, respectively, for the homemade ZAB. For comparison, a ZAB with a Pt/C catalyst as the cathode catalyst was also assembled. The discharge and cycling performance of the ZABs were evaluated using a CHI 760 electrochemical station (CH Instruments, Austin, TX, USA) and Neware BTS7.6 battery (Neware Technology Ltd., Shenzhen, China) evaluation system. Charge and discharge cycling measurements were conducted at the current density of 10 mA cm<sup>-2</sup>, with a fixed time interval of 5 min for each charge–discharge step.

**Author Contributions:** R.Y.: data curation, writing—original draft, and funding acquisition. W.X.: conceptualization and funding acquisition. L.P.: methodology and formal analysis. R.L.: validation and formal analysis. C.X.: methodology and formal analysis. X.Q.: conceptualization, writing—review and editing, and funding acquisition. All authors have read and agreed to the published version of the manuscript.

**Funding:** This research was funded by Guangdong Basic and Applied Basic Research Foundation (2020A1515110595, 2021A1515111076), Dongguan Science and Technology of Social Development Program (20221800905122), Dongguan Sci-tech Commissioner Program. (20231800500202), and the Innovation and Entrepreneurship Program for college students at Dongguan University of Technology (202211819255, 202211819251).

**Data Availability Statement:** The data presented in this study are available on request from the corresponding author.

**Conflicts of Interest:** The authors declare no conflict of interest.

## References

1. Lee, J.-S.; Kim, S.T.; Cao, R.; Choi, N.-S.; Liu, M.; Lee, K.T.; Cho, J. Metal-Air Batteries with High Energy Density: Li-Air versus Zn-Air. *Adv. Energy Mater.* **2011**, *1*, 34–50. [[CrossRef](#)]
2. Li, P.; Wei, B.; Lü, Z.; Wu, Y.; Zhang, Y.; Huang, X.  $\text{La}_{1.7}\text{Sr}_{0.3}\text{Co}_{0.5}\text{Ni}_{0.5}\text{O}_{4+\delta}$  layered perovskite as an efficient bifunctional electrocatalyst for rechargeable zinc-air batteries. *Appl. Surf. Sci.* **2019**, *464*, 494–501. [[CrossRef](#)]
3. Li, Y.; Dai, H. Recent advances in zinc-air batteries. *Chem. Soc. Rev.* **2014**, *43*, 5257–5275. [[CrossRef](#)] [[PubMed](#)]
4. Wu, F.; Dong, Y.; Su, Y.; Wei, C.; Chen, T.; Yan, W.; Ma, S.; Ma, L.; Wang, B.; Chen, L.; et al. Benchmarking the Effect of Particle Size on Silicon Anode Materials for Lithium-Ion Batteries. *Small* **2023**, e2301301. [[CrossRef](#)] [[PubMed](#)]
5. Asmontas, S.; Mujahid, M. Recent Progress in Perovskite Tandem Solar Cells. *Nanomaterials* **2023**, *13*, 1886. [[CrossRef](#)] [[PubMed](#)]
6. Miao, H.; Wang, Z.; Wang, Q.; Sun, S.; Xue, Y.; Wang, F.; Zhao, J.; Liu, Z.; Yuan, J. A new family of Mn-based perovskite ( $\text{La}_{1-x}\text{Y}_x\text{MnO}_3$ ) with improved oxygen electrocatalytic activity for metal-air batteries. *Energy* **2018**, *154*, 561–570. [[CrossRef](#)]
7. Ge, X.; Sumboja, A.; Wu, D.; An, T.; Li, B.; Goh, F.W.T.; Hor, T.S.A.; Zong, Y.; Liu, Z. Oxygen Reduction in Alkaline Media: From Mechanisms to Recent Advances of Catalysts. *ACS Catal.* **2015**, *5*, 4643–4667. [[CrossRef](#)]
8. Tan, P.; Chen, B.; Xu, H.; Zhang, H.; Cai, W.; Ni, M.; Liu, M.; Shao, Z. Flexible Zn- and Li-air batteries: Recent advances, challenges, and future perspectives. *Energy Environ. Sci.* **2017**, *10*, 2056–2080. [[CrossRef](#)]
9. Fu, C.; Ma, Q.; Wu, Q.; Yuan, Z.; Wu, Z.; He, J.; Li, X. Boosting bifunctional catalytic activity of perovskite nanoparticles for rechargeable Zn-air batteries. *Mater. Chem. Phys.* **2022**, *290*, 126557. [[CrossRef](#)]
10. Jung, K.N.; Jung, J.H.; Im, W.B.; Yoon, S.; Shin, K.H.; Lee, J.W. Doped lanthanum nickelates with a layered perovskite structure as bifunctional cathode catalysts for rechargeable metal-air batteries. *ACS Appl. Mater. Interfaces* **2013**, *5*, 9902–9907. [[CrossRef](#)]
11. Xue, Y.; Miao, H.; Sun, S.; Wang, Q.; Li, S.; Liu, Z.  $(\text{La}_{1-x}\text{Sr}_x)_{0.98}\text{MnO}_3$  perovskite with A-site deficiencies toward oxygen reduction reaction in aluminum-air batteries. *J. Power Sources* **2017**, *342*, 192–201. [[CrossRef](#)]
12. Cheng, F.; Chen, J. Metal-air batteries: From oxygen reduction electrochemistry to cathode catalysts. *Chem. Soc. Rev.* **2012**, *41*, 2172–2192. [[CrossRef](#)]
13. Zamani-Meymian, M.R.; Chenab, K.K.; Pourzolfaghar, H. Designing High-Quality Electrocatalysts Based on  $\text{CoO}:\text{MnO}_2@\text{C}$  Supported on Carbon Cloth Fibers as Bifunctional Air Cathodes for Application in Rechargeable Zn-Air Battery. *ACS Appl. Mater. Interfaces* **2022**, *14*, 55594–55607. [[CrossRef](#)]
14. Liu, X.; Zhang, G.; Wang, L.; Fu, H. Structural Design Strategy and Active Site Regulation of High-Efficient Bifunctional Oxygen Reaction Electrocatalysts for Zn-Air Battery. *Small* **2021**, *17*, e2006766. [[CrossRef](#)] [[PubMed](#)]
15. Zhang, J.; Zhao, Z.; Xia, Z.; Dai, L. A metal-free bifunctional electrocatalyst for oxygen reduction and oxygen evolution reactions. *Nat. Nanotechnol.* **2015**, *10*, 444–452. [[CrossRef](#)] [[PubMed](#)]
16. Suntivich, J.; Gasteiger, H.A.; Yabuuchi, N.; Nakanishi, H.; Goodenough, J.B.; Shao-Horn, Y. Design principles for oxygen-reduction activity on perovskite oxide catalysts for fuel cells and metal-air batteries. *Nat. Chem.* **2011**, *3*, 546–550. [[CrossRef](#)]
17. Cheng, Y.; Dou, S.; Veder, J.P.; Wang, S.; Saunders, M.; Jiang, S.P. Efficient and Durable Bifunctional Oxygen Catalysts Based on  $\text{NiFeO}@\text{MnO}_x$  Core-Shell Structures for Rechargeable Zn-Air Batteries. *ACS Appl. Mater. Interfaces* **2017**, *9*, 8121–8133. [[CrossRef](#)] [[PubMed](#)]
18. Han, X.; Cheng, F.; Zhang, T.; Yang, J.; Hu, Y.; Chen, J. Hydrogenated uniform Pt clusters supported on porous  $\text{CaMnO}_3$  as a bifunctional electrocatalyst for enhanced oxygen reduction and evolution. *Adv. Mater.* **2014**, *26*, 2047–2051. [[CrossRef](#)]
19. Li, C.; Baek, J.B. Recent Advances in Noble Metal (Pt, Ru, and Ir)-Based Electrocatalysts for Efficient Hydrogen Evolution Reaction. *ACS Omega* **2020**, *5*, 31–40. [[CrossRef](#)]
20. Nie, Y.; Li, L.; Wei, Z. Recent advancements in Pt and Pt-free catalysts for oxygen reduction reaction. *Chem. Soc. Rev.* **2015**, *44*, 2168–2201. [[CrossRef](#)] [[PubMed](#)]
21. Reier, T.; Oezaslan, M.; Strasser, P. Electrocatalytic Oxygen Evolution Reaction (OER) on Ru, Ir, and Pt Catalysts: A Comparative Study of Nanoparticles and Bulk Materials. *ACS Catal.* **2012**, *2*, 1765–1772. [[CrossRef](#)]

22. Zhang, Y.L.; Goh, K.; Zhao, L.; Sui, X.L.; Gong, X.F.; Cai, J.J.; Zhou, Q.Y.; Zhang, H.D.; Li, L.; Kong, F.R.; et al. Advanced non-noble materials in bifunctional catalysts for ORR and OER toward aqueous metal-air batteries. *Nanoscale* **2020**, *12*, 21534–21559. [[CrossRef](#)]
23. Qian, Y.; Hu, Z.; Ge, X.; Yang, S.; Peng, Y.; Kang, Z.; Liu, Z.; Lee, J.Y.; Zhao, D. A metal-free ORR/OER bifunctional electrocatalyst derived from metal-organic frameworks for rechargeable Zn-Air batteries. *Carbon* **2017**, *111*, 641–650. [[CrossRef](#)]
24. Dai, L.; Liu, M.; Song, Y.; Liu, J.; Wang, F. Mn<sub>3</sub>O<sub>4</sub>-decorated Co<sub>3</sub>O<sub>4</sub> nanoparticles supported on graphene oxide: Dual electrocatalyst system for oxygen reduction reaction in alkaline medium. *Nano Energy* **2016**, *27*, 185–195. [[CrossRef](#)]
25. Ishihara, T.; Guo, L.M.; Miyano, T.; Inoishi, Y.; Kaneko, K.; Ida, S. Mesoporous La<sub>0.6</sub>Ca<sub>0.4</sub>CoO<sub>3</sub> perovskites with large surface areas as stable air electrodes for rechargeable Zn-air batteries. *J. Mater. Chem. A* **2018**, *6*, 7686–7692. [[CrossRef](#)]
26. Xu, J.; Chen, C.; Han, Z.; Yang, Y.; Li, J.; Deng, Q. Recent Advances in Oxygen Electrocatalysts Based on Perovskite Oxides. *Nanomaterials* **2019**, *9*, 1161. [[CrossRef](#)]
27. Risch, M.; Stoerzinger, K.A.; Maruyama, S.; Hong, W.T.; Takeuchi, I.; Shao-Horn, Y. La<sub>0.8</sub>Sr<sub>0.2</sub>MnO<sub>3-delta</sub> decorated with Ba<sub>0.5</sub>Sr<sub>0.5</sub>Co<sub>0.8</sub>Fe<sub>0.2</sub>O<sub>3-delta</sub>: A bifunctional surface for oxygen electrocatalysis with enhanced stability and activity. *J. Am. Chem. Soc.* **2014**, *136*, 5229–5232. [[CrossRef](#)]
28. Kolla, P.; Nasymov, G.; Rajappagowda, R.; Smirnova, A. Bi-functionality of samarium- and praseodymium-based perovskite catalysts for oxygen reduction and oxygen evolution reactions in alkaline medium. *J. Power Sources* **2020**, *446*, 227234. [[CrossRef](#)]
29. Hwang, J.; Rao, R.R.; Giordano, L.; Katayama, Y.; Yu, Y.; Shao-Horn, Y. Perovskites in catalysis and electrocatalysis. *Science* **2017**, *358*, 751–756. [[CrossRef](#)] [[PubMed](#)]
30. Xu, N.; Yu, L.; Zhang, J.; Feng, J.; Zhao, L. Engineering of the A-site deficiency in La<sub>0.4</sub>Sr<sub>0.6</sub>Co<sub>0.7</sub>Fe<sub>0.2</sub>Nb<sub>0.1</sub>O<sub>3-δ</sub> perovskites for enhanced electrocatalytic oxygen reduction reaction. *J. Electroanal. Chem.* **2022**, *926*, 116936. [[CrossRef](#)]
31. Lu, Z.; Zhou, H.; Qian, B.; Wang, S.; Zheng, Y.; Ge, L.; Chen, H. Y and Fe co-doped LaNiO<sub>3</sub> perovskite as a novel bifunctional electrocatalyst for rechargeable zinc-air batteries. *Int. J. Hydrogen Energy* **2023**, *48*, 8082–8092. [[CrossRef](#)]
32. Lu, Y.; Ma, A.; Yu, Y.; Tan, R.; Liu, C.; Zhang, P.; Liu, D.; Gui, J. Engineering Oxygen Vacancies into LaCoO<sub>3</sub> Perovskite for Efficient Electrocatalytic Oxygen Evolution. *ACS Sustain. Chem. Eng.* **2018**, *7*, 2906–2910. [[CrossRef](#)]
33. Liu, K.; Li, J.; Wang, Q.; Wang, X.; Qian, D.; Jiang, J.; Li, J.; Chen, Z. Designed synthesis of LaCoO<sub>3</sub>/N-doped reduced graphene oxide nanohybrid as an efficient bifunctional electrocatalyst for ORR and OER in alkaline medium. *J. Alloys Compd.* **2017**, *725*, 260–269. [[CrossRef](#)]
34. Jiang, X.; Dong, Y.; Zhang, Z.; Li, J.; Qian, J.; Gao, D. Cation substitution of B-site in LaCoO<sub>3</sub> for bifunctional oxygen electrocatalytic activities. *J. Alloys Compd.* **2021**, *878*, 160433. [[CrossRef](#)]
35. Chandrappa, S.G.; Moni, P.; Chen, D.; Karkera, G.; Prakasha, K.R.; Caruso, R.A.; Prakash, A.S. The influence of ruthenium substitution in LaCoO<sub>3</sub> towards bi-functional electrocatalytic activity for rechargeable Zn-air batteries. *J. Mater. Chem. A* **2020**, *8*, 20612–20620. [[CrossRef](#)]
36. Qian, J.; Li, J.; Xia, B.; Zhang, J.; Zhang, Z.; Guan, C.; Gao, D.; Huang, W. Multi-stability modulating of alkaline-earth metal doped LaCoO<sub>3</sub> for rechargeable Zn-air batteries. *Energy Storage Mater.* **2021**, *42*, 470–476. [[CrossRef](#)]
37. Zhou, H.; Zhao, W.; Lu, Z.; He, S.; Yin, B.; Zheng, Y.; Ge, L.; Chen, H. Ba-doped LaCoO<sub>3</sub> perovskite as novel bifunctional electrocatalyst for zinc-air batteries. *Electrochim. Acta* **2023**, *462*, 142757. [[CrossRef](#)]
38. Shin, B.; Choi, S. Electrocatalytic Activity of Co-based Perovskite Oxides for Oxygen Reduction and Evolution Reactions. *Int. J. Electrochem. Sci.* **2016**, *11*, 5900–5908. [[CrossRef](#)]
39. Ananyev, M.V.; Porotnikova, N.M.; Kurumchin, E.K. Influence of strontium content on the oxygen surface exchange kinetics and oxygen diffusion in La<sub>1-x</sub>Sr<sub>x</sub>CoO<sub>3-δ</sub> oxides. *Solid State Ion.* **2019**, *341*, 115052. [[CrossRef](#)]
40. Wang, M.; Han, B.; Deng, J.; Jiang, Y.; Zhou, M.; Lucero, M.; Wang, Y.; Chen, Y.; Yang, Z.; N'Diaye, A.T.; et al. Influence of Fe Substitution into LaCoO<sub>3</sub> Electrocatalysts on Oxygen-Reduction Activity. *ACS Appl. Mater. Interfaces* **2019**, *11*, 5682–5686. [[CrossRef](#)] [[PubMed](#)]
41. Vignesh, A.; Prabu, M.; Shanmugam, S. Porous LaCo<sub>1-x</sub>Ni<sub>x</sub>O<sub>3-delta</sub> Nanostructures as an Efficient Electrocatalyst for Water Oxidation and for a Zinc-Air Battery. *ACS Appl. Mater. Interfaces* **2016**, *8*, 6019–6031. [[CrossRef](#)] [[PubMed](#)]
42. Zhang, C.; Cui, Y.; Ke, W.; Liang, Y.; Chao, Y.; Han, N.; Liang, P.; He, X. Enhanced cycling stability of La<sub>0.2</sub>Sr<sub>0.8</sub>CoO<sub>3-δ</sub> for oxygen evolution reaction via trace doping of Nb. *Ceram. Int.* **2022**, *48*, 36992–36999. [[CrossRef](#)]
43. Wang, C.C.; Cheng, Y.; Ianni, E.; Jiang, S.P.; Lin, B. A highly active and stable La<sub>0.5</sub>Sr<sub>0.5</sub>Ni<sub>0.4</sub>Fe<sub>0.6</sub>O<sub>3-δ</sub> perovskite electrocatalyst for oxygen evolution reaction in alkaline media. *Electrochim. Acta* **2017**, *246*, 997–1003. [[CrossRef](#)]
44. Feng, X.; Fan, Y.; Nomura, N.; Kikuchi, K.; Wang, L.; Jiang, W.; Kawasaki, A. Graphene promoted oxygen vacancies in perovskite for enhanced thermoelectric properties. *Carbon* **2017**, *112*, 169–176. [[CrossRef](#)]
45. Yuan, R.-H.; He, Y.; He, W.; Ni, M.; Leung, M.K.H. Bifunctional electrocatalytic activity of La<sub>0.8</sub>Sr<sub>0.2</sub>MnO<sub>3</sub>-based perovskite with the A-site deficiency for oxygen reduction and evolution reactions in alkaline media. *Appl. Energy* **2019**, *251*, 113406. [[CrossRef](#)]

**Disclaimer/Publisher's Note:** The statements, opinions and data contained in all publications are solely those of the individual author(s) and contributor(s) and not of MDPI and/or the editor(s). MDPI and/or the editor(s) disclaim responsibility for any injury to people or property resulting from any ideas, methods, instructions or products referred to in the content.